The Community Code Verification Exercise for Simulating Sequences of Earthquakes and Aseismic Slip (SEAS)

Brittany A. Erickson*[1], Junle Jiang[2], Michael Barall[3], Nadia Lapusta[4], Eric M. Dunham[5], Ruth Harris[6], Lauren S. Abrahams[5], Kali L. Allison[7], Jean-Paul Ampuero[8], Sylvain Barbot[9], Camilla Cattania[5], Ahmed Elbanna[10], Yuri Fialko[11], Benjamin Idini[4], Jeremy E. Kozdon[12], Valère Lambert[4], Yajing Liu[13], Yingdi Luo[4], Xiao Ma[10], Maricela Best McKay[14], Paul Segall[5], Pengcheng Shi[15], Martijn van den Ende[8], and Meng Wei[15]

Abstract

Numerical simulations of sequences of earthquakes and aseismic slip (SEAS) have made great progress over past decades to address important questions in earthquake physics. However, significant challenges in SEAS modeling remain in resolving multiscale interactions between earthquake nucleation, dynamic rupture, and aseismic slip, and understanding physical factors controlling observables such as seismicity and ground deformation. The increasing complexity of SEAS modeling calls for extensive efforts to verify codes and advance these simulations with rigor, reproducibility, and broadened impact. In 2018, we initiated a community code-verification exercise for SEAS simulations, supported by the Southern California Earthquake Center. Here, we report the findings from our first two benchmark problems (BP1 and BP2), designed to verify different computational methods in solving a mathematically well-defined, basic faulting problem. We consider a 2D antiplane problem, with a 1D planar vertical strike-slip fault obeying rate-and-state friction, embedded in a 2D homogeneous, linear elastic half-space. Sequences of quasi-dynamic earthquakes with periodic occurrences (BP1) or bimodal sizes (BP2) and their interactions with aseismic slip are simulated. The comparison of results from 11 groups using different numerical methods show excellent agreements in long-term and coseismic fault behavior. In BP1, we found that truncated domain boundaries influence interseismic stressing, earthquake recurrence, and coseismic rupture, and that model agreement is only achieved with sufficiently large domain sizes. In BP2, we found that complexity of fault behavior depends on how well physical length scales related to spontaneous nucleation and rupture propagation are resolved. Poor numerical resolution can result in artificial complexity, impacting simulation results that are of potential interest for characterizing seismic hazard such as earthquake size distributions, moment release, and recurrence times. These results inform the development of more advanced SEAS models, contributing to our further understanding of earthquake system dynamics.

Cite this article as Erickson, B. A., J. Jiang, M. Barall, N. Lapusta, E. M. Dunham, R. Harris, L. S. Abrahams, K. L. Allison, J.-P. Ampuero, S. Barbot, *et al.* (2020). The Community Code Verification Exercise for Simulating Sequences of Earthquakes and Aseismic Slip (SEAS), *Seismol. Res. Lett.* **91**, 874–890, doi: 10.1785/0220190248.

Introduction and Motivation

When we develop models of physical systems, credible and reproducible results are essential to scientific progress. Robust forward models of earthquake source processes have become important means for studying fundamental questions in earthquake science. Models of single earthquakes (known as dynamic rupture simulations) have emerged as powerful tools for understanding the influence of fault geometry, friction, and prestress on rupture propagation, and for explaining observations of high-frequency ground motions and damage zones

1. University of Oregon, Eugene, Oregon, U.S.A.; 2. Cornell University, Ithaca, New York, U.S.A.; 3. Invisible Software, Inc., San Jose, California, U.S.A.; 4. California Institute of Technology, Pasadena, California, U.S.A.; 5. Stanford University, Stanford, California, U.S.A.; 6. U.S. Geological Survey, Moffett Field, California, U.S.A.; 7. University of Maryland, College Park, Maryland, U.S.A.; 8. Université Côte d'Azur, IRD, CNRS, Observatoire de la Côte d'Azur, Géoazur, Valbonne, France; 9. University of Southern California, Los Angeles, California, U.S.A.; 10. University of Illinois Urbana-Champaign, Urbana, Illinois, U.S.A.; 11. University of California San Diego, La Jolla, California, U.S.A.; 12. Naval Postgraduate School, Monterey, California, U.S.A.; 13. McGill University, Montreal, Quebec, Canada; 14. Portland State University, Portland, Oregon, U.S.A.; 15. University of Rhode Island, Narragansett, Rhode Island, U.S.A.

*Corresponding author: bae@uoregon.edu

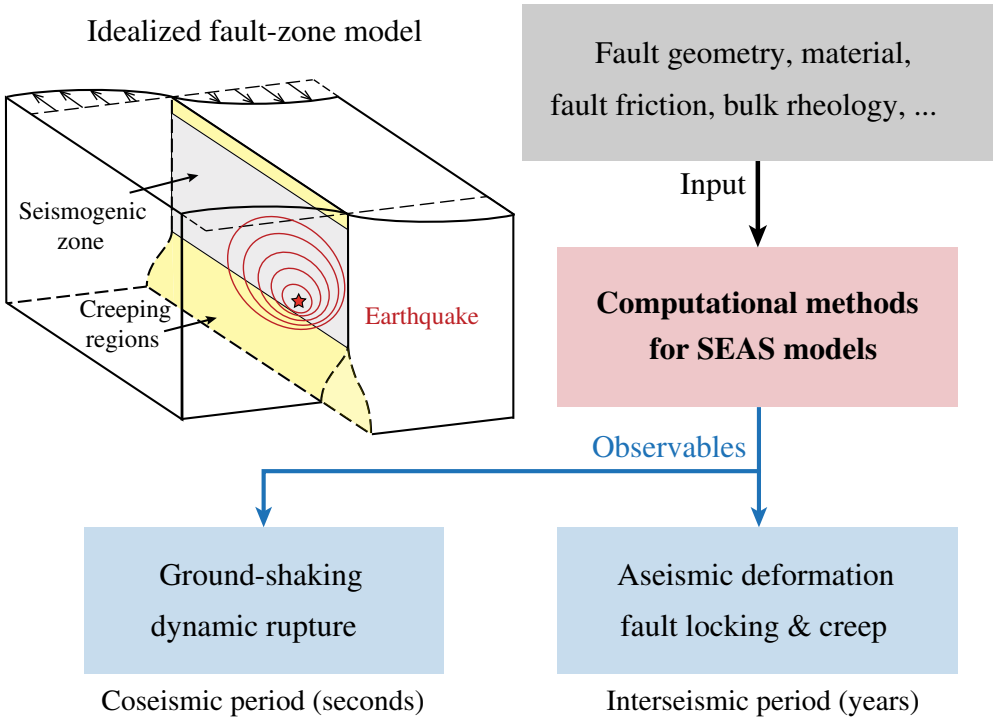

Figure 1. Ingredients and observables for sequences of earthquakes and aseismic slip (SEAS) models. In a conceptual fault-zone model, earthquakes initiate at seismogenic depths (red star) and rupture through the interseismically locked regions (gray), whereas aseismic slip occurs in deeper and sometimes shallower regions (yellow). For numerical models, given fault-zone properties, computational simulations can reproduce long-term fault locking and creep over years to decades, punctuated by dynamic earthquake ruptures over seconds to minutes. Seismic shaking and aseismic deformation are typical observables from the surface. The color version of this figure is available only in the electronic edition.

(Day, 1982; Olsen *et al.*, 1997; Nielsen *et al.*, 2000; Duan and Oglesby, 2006; Bhat *et al.*, 2007; Ripperger *et al.*, 2007; Dunham *et al.*, 2011a,b; Lozos *et al.*, 2011; Gabriel *et al.*, 2012; Kozdon and Dunham, 2013; Shi and Day, 2013; Xu *et al.*, 2015; Ma and Elbanna, 2019; Wollherr *et al.*, 2019). Confidence in model outcomes produced by these codes has been boosted significantly over the past decade through the code comparison studies done by the Southern California Earthquake Center/U.S. Geological Survey (SCEC/USGS) Spontaneous Rupture Code Verification Project (Harris *et al.*, 2009, 2018; Barall and Harris, 2015).

Although these dynamic rupture simulations have contributed greatly to our understanding of the physical factors that govern ground motion, they are limited to single-event scenarios and often impose artificial prestress conditions and *ad hoc* nucleation procedures. Although some recent methods have been proposed to infer initial prestress distributions from geophysical observations (Aochi and Twardzik, 2019; Gallovic *et al.*, 2019; Yang *et al.*, 2019) or geodynamic modeling (van Zelst *et al.*, 2019) for specific settings, generic, and physics-based strategies for estimating the prestress in the context of recurring earthquakes is still lacking and crucially important. To understand earthquake source processes and how fault-slip history influences subsequent events, it has been widely recognized that we need models that simulate behavior over multiple seismic events and the intervening periods of aseismic deformation. To address this need, models of sequences of earthquakes and aseismic slip (SEAS) have emerged that consider all phases of earthquake faulting, from slow tectonic loading to earthquake nucleation (under self-consistent prestress conditions), propagation, and termination. However, so far codes for SEAS simulations remain untested. Inspired by the success of the SCEC/USGS Spontaneous Rupture Code Verification Project, this article describes the efforts of the SEAS initiative—a SCEC funded working group who has initiated the first code-verification study for earthquake sequence simulations. In this article, we present the initial benchmark problems and results from the code comparisons submitted to our online platform (see Data and Resources). Through these exercises, we aim to provide confidence in SEAS model outcomes, determine best practices for improvement of accuracy and efficiency of SEAS simulations, and provide other scientists strategies for verification during code development.

In SEAS models, the goal is to capture the interplay of interseismic periods and the associated aseismic fault slip that ultimately lead to earthquake nucleation and earthquakes (dynamic rupture events) themselves, in an effort to understand which physical factors control the full range of observables such as aseismic deformation, nucleation locations of earthquakes, ground shaking during dynamic rupture, recurrence times, and magnitudes of major earthquakes (see Fig. 1). These features distinguish SEAS models from both dynamic rupture models that only consider single events and the so-called earthquake simulators (Tullis *et al.*, 2012). Earthquake simulators are capable of simulating seismicity patterns over millennium time scales in complex fault network systems (Richards-Dinger and Dieterich, 2012) but often adopt semi-kinematic elements (e.g., the imposition of back-slip loading to

account for external sources of stress, see Tullis *et al.*, 2012) and are missing key physical features that could potentially dominate earthquake and fault interaction such as stress transfer generated by seismic waves, aseismic slip within fault segments, and inelastic off-fault responses.

SEAS modeling is not without significant challenges, due to the varying temporal and spatial scales that characterize earthquake source behavior. For computational efficiency, the vast majority of SEAS models do not consider full dynamics during earthquake rupture, but rather take a quasi-dynamic approach, in which inertia is only approximated (see the next section for further details). Computations are further complicated when material heterogeneities, bulk inelastic responses, and fault nonplanarity are included. However, accounting for such complexity is widely recognized as crucial for understanding the real Earth and assessing seismic hazards. Significant developments in SEAS models over the past decade have incorporated some of these complexities and connected model outcomes to geophysical observations. For example, seismological and geodetic observations have been combined with modeling of coseismic and quasi-static (aseismic) deformation to infer the spatial distribution of fault frictional properties (Johnson *et al.*, 2006; Barbot *et al.*, 2009; Mitsui and Hirahara, 2011; Dublanchet *et al.*, 2013; Floyd *et al.*, 2016; Jiang and Fialko, 2016), the decay rate of aftershocks (Perfettini and Avouac, 2004, 2007), the role of tremor and slow slip (Mele Veedu and Barbot, 2016; Dublanchet, 2017; Luo and Ampuero, 2017), and long-term models have been used to reproduce characteristics of multiple and/or repeating events (Chen and Lapusta, 2009; Barbot *et al.*, 2012). The framework of earthquake cycle modeling is also adopted to explain geodetic and geologic data (Kaneko *et al.*, 2011; Meade *et al.*, 2013; Wei *et al.*, 2013, 2018), study subduction zones (Hori *et al.*, 2004; Liu and Rice, 2005, 2007; Noda and Lapusta, 2013; van Dinther *et al.*, 2013; Li and Liu, 2016, 2017), collision zones (Qiu *et al.*, 2016; Michel *et al.*, 2017), and explore induced seismicity phenomena (McClure and Horne, 2011; Dieterich *et al.*, 2015), among many applications.

Although SEAS models are being used to explain, reproduce, and predict earthquake behavior and other geophysical phenomena, a critical step must be to ensure that these methodologies are accurate. The SEAS initiative is also taking the step to improve and promote a new generation of verified numerical SEAS models that can simulate much longer periods of earthquake activity than single-event dynamic rupture simulations but with the same level of computational rigor, while incorporating qualitatively different features such as (a) pre-, inter-, and postseismic slip and the resulting stress redistribution, (b) spontaneous earthquake nucleation, and (c) physical processes relevant to long-term slip such as interseismic healing of the fault zone, viscoelasticity, and fluid flow. Such SEAS models can provide physics-based approximations for larger-scale and longer-term earthquake simulators and also inform the initial conditions and nucleation procedures for dynamic rupture simulations. Our vision for SEAS models is to extend them to include full dynamic ruptures, capturing the range of processes and heterogeneities known to be essential for realistic modeling of earthquake source processes and ground motion.

SEAS Modeling Challenges and Initial Benchmark Problems

Although the ultimate SEAS modeling framework would naturally include dynamic rupture modeling, current methods for simulating SEAS problems require computational codes that are fundamentally different from those used in single-event dynamic rupture simulations. The use of variable time stepping and possible switching between different computational schemes is required to resolve subseconds to year-long changes. The interaction between the highly nonlinear nature of the problems and round-off errors can lead to model divergence. The need to distinguish between legitimate solution differences versus those due to improper choices of algorithm and modeling procedures necessitates new and more suitable comparison metrics.

SEAS models are unique in that they cover a wide range of numerical methodologies and applications in earthquake science. Methods based on spectral boundary integral formulations boundary integral equation method (BIEM) are efficient in solving for earthquake ruptures with quasi dynamic or full inertial effects (Lapusta and Rice, 2003; Lapusta and Liu, 2009; Jiang and Lapusta, 2016). Methods based on the finite-difference method (FDM) or a hybrid finite element-spectral BIEM have been used to simulate quasi-dynamic ruptures on faults with more complex bulk rheologies (Erickson and Dunham, 2014; Erickson *et al.*, 2017; Allison and Dunham, 2018; Abdelmeguid *et al.*, 2019; Mckay *et al.*, 2019). Other SEAS modeling approaches include boundary element methods (BEMs) for simulating slow slip and tremor (e.g., Rice and Tse, 1986; Tse and Rice, 1986; Luo and Ampuero, 2011; Nakata *et al.*, 2012; Liu, 2013; Wei *et al.*, 2013; Goswami and Barbot, 2018; Ong *et al.*, 2019), coupling faulting with fluid and heat transport and inelastic dilatancy (Segall and Bradley, 2012a), effects of surface topography (Ohtani and Hirahara, 2015), frictional heterogeneities (Kato, 2016), and viscoelastic response (Kato, 2002; Lambert and Barbot, 2016; Barbot, 2018). A spectral element method has also been developed for simulating fully dynamic earthquakes in a heterogeneous bulk (Kaneko *et al.*, 2010).

To verify the accuracy of SEAS models based on these different computational methods, the SEAS group developed our first benchmark problem BP1 to test the capabilities of different computational methods in correctly solving a mathematically well-defined problem in crustal faulting. The overall strategy of our benchmark exercises is to produce robust results and maximize participation, with the goal of obtaining agreements in resolving detailed fault-slip history over a range of time scales. These efforts required us to better understand

the dependence of fault-slip history on initial conditions, model spin-up, fault properties, and friction laws. Given the complexity of this task, it was important to start from the most basic problem and gradually add model complexity. BP1 is a 2D antiplane problem, with a 1D planar vertical strike-slip fault embedded in a 2D homogeneous, linear elastic half-space with a free surface (see Fig. 2). Full details of this benchmark (and subsequent benchmarks), including governing equations and initial and fault interface conditions, are available online on the SEAS platform (see Data and Resources). We include some of the details on the friction law here, for clarity of important concepts.

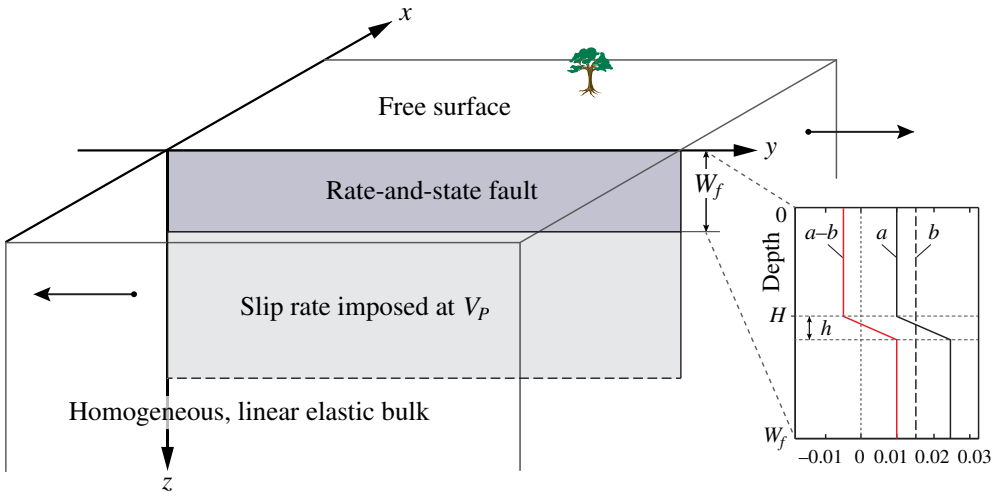

Figure 2. Our first SEAS benchmark is based on the model in Rice (1993), in which a planar fault is embedded in a homogeneous, linear elastic half-space with a free surface. A vertical cross section of the 3D setting is taken so that slip varies only with depth and deformation is 2D antiplane strain. The fault is governed by rate-and-state friction with depth-dependent frictional parameters a and b above the depth W_f, below which a steady slow loading rate V_P is assumed. The friction-controlled fault is seismogenic due to velocity-weakening (VW) properties ($(a-b)<0$) down to depth H and accommodates aseismic creep at greater depths due to velocity-strengthening (VS) properties ($(a-b)>0$). Earthquakes nucleate spontaneously, with inertia approximated with radiation damping. The color version of this figure is available only in the electronic edition.

The fault is governed by rate- and state-dependent friction (Dieterich, 1979; Ruina, 1983; Marone, 1998) in which shear stress on the fault τ is set equal to fault strength F, namely

$$\tau = F(V,\theta), \tag{1}$$

in which $\tau = \tau^0 + \tau^{qs} - \eta V$ is the sum of the prestress τ^0, the shear stress due to quasi-static deformation τ^{qs}, and the radiation damping term $-\eta V$ as approximation to inertia (Rice, 1993). $\eta = \mu/2c_s$ is half the shear-wave impedance for shear-wave speed $c_s = \sqrt{\mu/\rho}$, in which μ is the elastic shear modulus and ρ is the material density. The fault strength $F = \sigma_n f(V,\theta)$, in which V is the slip rate and θ is a state variable. σ_n is the effective normal stress on the fault. For this first benchmark problem, we assume θ evolves according to the aging law

$$\frac{d\theta}{dt} = 1 - \frac{V\theta}{L}, \tag{2}$$

in which L is the critical slip distance. The friction coefficient f is given by a regularized formulation (Lapusta *et al.*, 2000):

$$f(V,\theta) = a\sinh^{-1}\left[\frac{V}{2V_0}\exp\left(\frac{f_0 + b\ln(V_0\theta/L)}{a}\right)\right], \tag{3}$$

for reference friction coefficient f_0 and reference slip rate V_0. Depth-dependent frictional parameters a and b define a shallow seismogenic region with velocity-weakening (VW) friction and a deeper velocity-strengthening (VS) region, below which a relative plate motion rate is imposed. A periodic sequence of spontaneous, quasi-dynamic earthquakes and slow slip are simulated in the model, see Figure 3a, in which results from the Boundary Integral Cycle of Earthquakes (BICyclE) code (Lapusta *et al.*, 2000; Lapusta and Liu, 2009) show-slip contours plotted against fault depth in blue every 5 yr during interseismic loading and in red every 1 s during the coseismic phase. Over a 1200 yr simulation period, approximately 13 events take place, nucleating at a depth of ~12 km, rupturing to a depth of ~18 km, and accumulating ~3 m of slip at the Earth's surface.

Model parameters used for the benchmark are given in Table 1. The adopted values for elasticity parameters ρ and c_s are within typical ranges for crustal rock types (Christensen, 1989; Tape *et al.*, 2009) and common in earthquake modeling (Noda *et al.*, 2009; Ma and Andrews, 2010; Dunham *et al.*, 2011a). Frictional parameters a and b are chosen such that $a-b$ is constant over the shallow, VW ($a-b<0$) region and the deeper VS ($a-b>0$) region, and follows a linear transition between the two regions. The values for a and b are chosen mainly for simplicity and largely consistent with laboratory-derived values for granite under hydrothermal conditions (Blanpied *et al.*, 1991; Rice, 1993). The choice of constant effective normal stress was taken for simplicity; depth-independent effective normal stress below a certain depth is a feature of

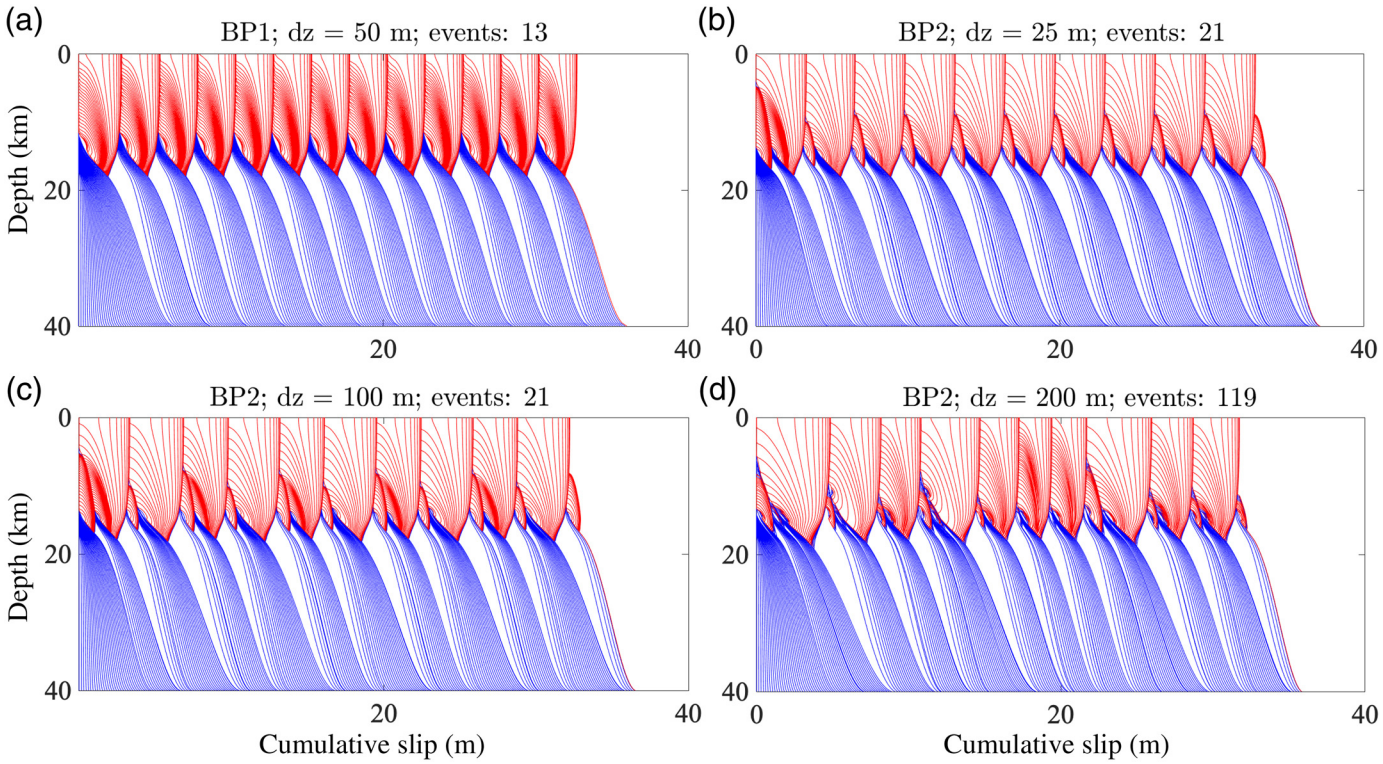

Figure 3. Cumulative slip profiles plotted over a 1200 yr period in blue every 5 yr during interseismic loading and in red every second during quasi-dynamic rupture. Results were obtained using the BICyclE code for (a) BP1 with a cell size of 50 m, (b) BP2 with a cell size of 25 m, (c) BP2 with a cell size of 100 m, and (d) BP2 with a cell size of 200 m. Number of events also listed, in which we define a seismic event to be one with a local slip rate >0.01 m/s separated by aseismic periods of at least 15 s. The color version of this figure is available only in the electronic edition.

some models under the assumption of high-fluid overpressurization at depth (Rice, 1992; Lapusta *et al.*, 2000). Laboratory values of the critical slip distance L are on the order of microns. We choose L to be several orders of magnitude larger, however, for computational tractability.

A critical physical length scale present in this first benchmark problem is the process zone Λ , which describes the spatial region near the rupture front under which breakdown of fault resistance occurs, and shrinks as ruptures propagate faster (Palmer and Rice, 1973). For fault models governed by rate-and-state friction, the quasi-static process zone at a rupture speed of 0^+, Λ_0, can be estimated (Day *et al.*, 2005; Ampuero and Rubin, 2008; Perfettini and Ampuero, 2008) as:

$$\Lambda_0 = C\frac{\mu L}{b\sigma_n}, \tag{4}$$

in which C is a constant of order 1. Another characteristic length scale that has been shown to control model behavior is the critical nucleation size h^*, which governs the minimum extent of the rate-weakening region under which spontaneous nucleation may occur, (see Andrews, 1976a,b; Rubin and Ampuero, 2005; Ampuero and Rubin, 2008). For 2D problems, the critical nucleation size can be estimated for the aging law (with $0.5 < a/b < 1$) as:

$$h^* = \frac{2}{\pi}\frac{\mu b L}{(b-a)^2\sigma_n}. \tag{5}$$

Throughout this work we use the term cell size to refer to model resolution, that is, the length between grid points. For numerical methods (such as high-order finite-element methods) that are not based on equally spaced grids, cell size should be interpreted as an average resolution per degree of freedom along the face of an element. For BP1 we suggested a cell size Δz of 25 m, resolving Λ_0 with approximately 12 grid points and h^* with approximately 80 grid points (i.e., $\Lambda_0/\Delta z \approx 12$, $h^*/\Delta z \approx 80$).

We developed the second benchmark BP2 that is similar to BP1 to explore the model resolution issues, which will be important in future benchmarks in 3D when computational efficiency demands a larger cell size. Complexity of event sizes and recurrence times is known to emerge through a reduction in the characteristic slip distance L (Lapusta and Rice, 2003; Mitsui and Hirahara, 2011; Kato, 2014; Wu and Chen, 2014; Viesca, 2016a,b; Barbot, 2019; Cattania, 2019). Thus BP2 is exactly the same as BP1 except that L is halved, resulting in bimodal sequences of full and partial ruptures of the VW region (every large event is accompanied by a smaller event and the sequence repeats periodically). Besides aiming for

TABLE 1
Parameter Values Used in the Benchmark Problem

Parameter	Definition	Value (Units)
ρ	Density	2670 kg/m^3
c_s	Shear-wave speed	3.464 km/s
σ_n	Effective normal stress on fault	50 MPa
a	Rate-and-state parameter	Variable (see Fig. 1)
b	Rate-and-state parameter	Variable (see Fig. 1)
L	Critical slip distance	BP1: 0.008 m; BP2: 0.004 m
V_P	Plate rate	10^{-9} m/s
V_{init}	Initial slip rate	10^{-9} m/s
V_0	Reference slip rate	10^{-6} m/s
f_0	Reference friction coefficient	0.6
H	Depth extent of uniform VW region	15 km
h	Width of VW–VS transition zone	3 km
W_f	Width of rate-and-state fault	40 km
Δz	Suggested cell sizes	BP1: 25 m; BP2: 25 m, 50 m, 100 m, 200 m, 300 m, 400 m, 800 m
t_f	Final simulation time	BP1: 3000 yr; BP2: 1200 yr
L_z	Depth of computational domain	Not specified
L_x	Off-fault distance of computational domain	Not specified

VS, velocity strengthening; VW, velocity weakening.

agreements between different models, one main objective is to understand complexity in simulated events and how to deal with numerical resolution issues. A reduction in L corresponds to a reduction in the quasi-static process zone size Λ_0. BP2 requests model outputs using a cell size of 25, 50, 100, 200, 300, 400, and 800 m. The first three cases resolve Λ_0 with approximately 6, 3, and 1.7 grid points, and the other four cases do not resolve Λ_0. Figure 3b–d shows results from the BICyclE code using a cell size of 25, 100, and 200 m, respectively. Small cell sizes of 25 and 50 m (the latter is not shown) show nearly indistinguishable, bimodal patterns of events nucleating at ~15 km depth, suggesting model convergence. A cell size of 100 m leads to a resolution issue where periodic behavior is observed, but the bimodal sequence of events is replaced by an alternating sequence of large-, small-, and medium-size events. A cell size of 200 m, which does not resolve the process zone, reveals a loss of periodic behavior altogether in favor of a broad range of event sizes and nucleation locations.

TABLE 2
Details of Participating SEAS Codes and Modeling Groups

Code Name	Type	Modeler Name and Group Members	References
SCycle	FDM	abrahams (Abrahams/Allison/Dunham)	Erickson and Dunham (2014), Allison and Dunham (2018), see Data and Resources
FDCycle	FDM	erickson (Erickson/Mckay)	Erickson and Dunham (2014), see Data and Resources
QDESDG	FEM	kozdon (Kozdon)	see Data and Resources
Unicycle	BEM	barbot (Barbot)	Barbot (2019)
FDRA	BEM	cattania (Cattania/Segall)	Segall and Bradley (2012b), Bradley (2014)
BICyclE	BEM	jiang (Jiang); lambert (Lambert/Lapusta); xma (Ma/Elbanna)	Lapusta *et al.* (2000), Lapusta and Liu (2009)
QDYN	BEM	luo (Luo/Idini/van den Ende/Ampuero)	Luo and Ampuero (2017), see Data and Resources
ESAM	BEM	liu (Liu); wei (Wei/Shi)	Liu and Rice (2007)

BEM, boundary element method; BICyclE, Boundary Integral Cycle of Earthquakes; ESAM, Earthquake Sequence and Aseismic Modeling; FDCycle, finite Difference method for earthquake Cycles; FDM, finite-difference method; FDRA, Fault dynamics with a radiation-damping approximation; FEM, finite element method; QDESDG, Quasi-Dynamic Earthquake Simulations with Discontinuous Galerkin methods; QDYN, Quasi-DYNamic earthquake simulator; SCycle, sequences of earthquake cycles; SEAS, sequences of earthquakes and aseismic slip.

Modeling Groups and Working Platforms

For these benchmark exercises, we have used two SCEC-funded workshops (hosted in April and November 2018, see Data and Resources) as open platforms for modelers to share and follow recent scientific progress in the field, discuss details in benchmark design and results, and collectively decide the directions of our future efforts, with considerable inputs from students and early career scientists. Eleven modeling groups participated in these first two benchmarks; the details of the group members and different computational methods are summarized in Table 2. The modeler name refers to the member of the modeling group who uploaded the data to the platform for simulations done by the group. It does not necessarily refer to the code author(s)—see the references in Table 2 for authorship and code availability. For time-stepping schemes, the majority of groups used adaptive Runge–Kutta methods for both benchmark problems (the details of which can be found in the references listed in Table 2), with the exception of Quasi-DYNamic earthquake simulator (QDYN), which applies a Bulirsch–Stoer method for BP1, and BICyclE, which incorporates adaptive time-stepping based on stability conditions derived from the choice of constitutive relationship.

(a)

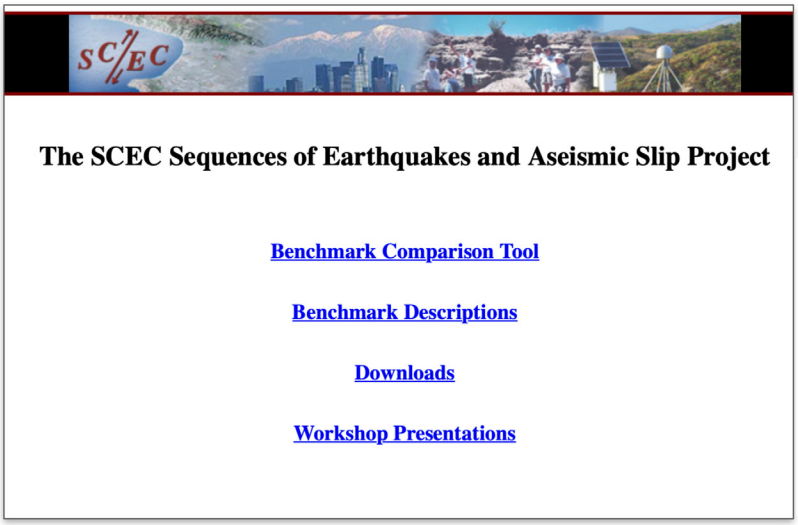

(b)

Benchmarks

Name	Date	Description	Action
bp1	4/14/2018 8:08 AM	2D Antiplane Shear	Select
bp2	10/6/2018 6:20 AM	2D Antiplane Shear, Varying Cell Size	Select

(c)

Users — Select Checked — Select All

	Name	Description	Action
☐	abrahams	100 km X 80 km: Free surface outer BC	Select
☐	abrahams.2	100 km X 80 km: Vp/2 outer BC	Select
☐	abrahams.3	400 km X 200 km: Vp/2 outer BC	Select
☐	barbot	Sylvain Barbot (Fortran90)	Select
☐	barbot.2	Sylvain Barbot (Matlab)	Select
☐	cattania	Camilla Cattania - fdra (bem)	Select
☐	cattania.2	Camilla Cattania - fdra (fft, 160 km)	Select
☐	cattania.3	Camilla Cattania - fdra (fft, 640 km)	Select
☐	erickson	Brittany Erickson	Select
☐	erickson.2	Brittany Erickson	Select

Figure 4. Online platform for the SEAS working group. (a) Home page for our website. (b) Currently available benchmarks. (c) Examples of BP1 model submissions. The color version of this figure is available only in the electronic edition.

To facilitate the submission and comparison of simulation results, we established an online platform that provides access to community resources and supports the submission, storage, visualization, and comparison of benchmark results (see Fig. 4). For our first benchmarks, we adopted a platform with similar functionality developed for the SCEC dynamic rupture simulation group (see Data and Resources). All modelers can upload and immediately plot time-series data to quickly assess the overall agreements between models for the time evolution of fault slip, slip rates, and shear stress at representative locations on fault. Although the online platform is currently limited to comparing time series, additional comparisons, like slip contours along depth, were made by the modeling groups to analyze more detailed model observables. In the future, we plan to add such functionality to the online platform.

Model Comparisons and What We Learned

It is important that the problem descriptions for BP1 and BP2 consider a semi-infinite half-space. Codes based on a volume discretization (FDM/finite-element method [FEM]) therefore had to make their own decisions regarding computational domain truncation and far-field boundary conditions (BCs). The figures in the following sections contain labels generated by the platform which state the model group name and correspond to results from a particular model setup. Some results are followed by the version corresponding to an alternative setup, for example, abrahams.3 corresponds to results from the abrahams group with an increased computational domain size of $(L_x, L_z) = (400\text{ km}, 200\text{ km})$ and a remote displacement BC, see the lower right of Figure 4. We discuss in the next sections the implications that these choices had on model comparisons.

Results from BP1

For the first benchmark problem BP1, we found qualitative agreements in nucleation sites, depth extent of rupture, and slip with depth similar to those exemplified by the slip contours in Figure 3a. In Figure 5, we plot time series of local shear stress and slip rates at midseismogenic depth ($z = 7.5$ km) from BP1 over the first 700 yr for different model results. Results from several BEM codes as well as codes with volume discretization (abrahams and kozdon modeling groups) and varying computational domain sizes are compared in Figure 5a,b. The legends indicate the computational domain size and BC. For BEM codes, HS refers to a half-space, and (L_z, BC) refers to computational domain depth and BC, in which BC3 corresponds to a periodic BC. For codes with a volume discretization, (L_x/L_z/BC) provides the computational domain size used and BC1 and BC2 refers to a far-field free surface or a far-field displacement BC, respectively.

Figure 5a,b shows model results from a BEM simulation (liu, in black) along with four model results from volume discretization codes, revealing quantitative differences in interevent times, and peak values. Interevent times for different models range from approximately 78.3 to 78.8 yr over the whole 3000 yr simulation period, leading to model divergence at a near-constant rate. We found that these discrepancies were caused by choices in domain truncation and BCs. We were surprised to find that far-field BC type leads to quantitative differences in long-term fault behavior for relatively small domains (revealed by the blue and orange curves in Fig. 5a,b). This in part is due to small differences in the physical problem being solved by implementations that use periodic or finite domain BCs compared to the spatial domain BEM methods, which represent a truly infinite domain, and therefore larger loading regions. The green and red curves in Figure 5a,b,

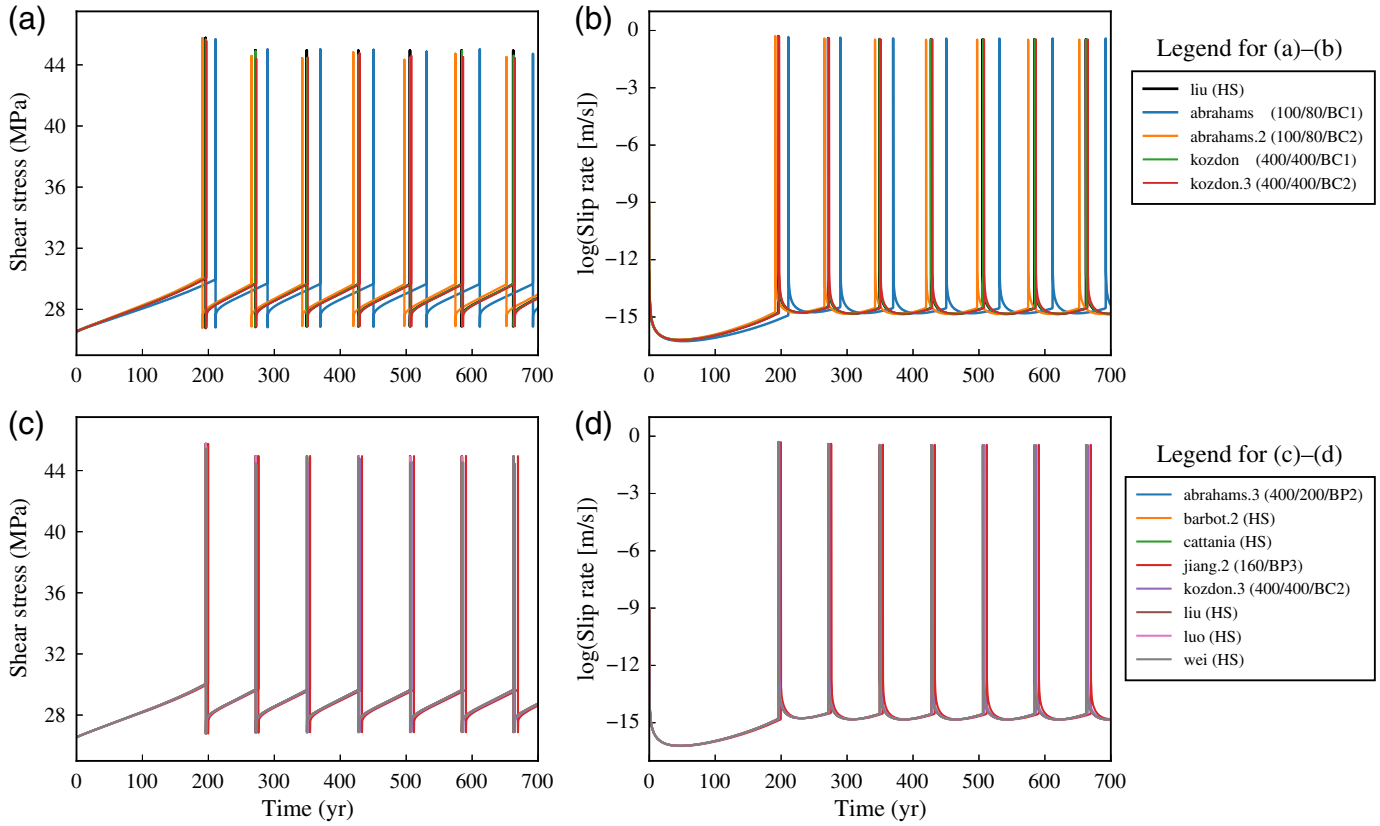

Figure 5. Long-term behavior of BP1 models. (a) Shear stress and (b) slip rates at the depth of 7.5 km in models with different outer boundary conditions (BC) and computational domain sizes. (c) Shear stress and (d) slip rates at depth of 7.5 km in models with sufficiently large computational domain sizes. Legend labels indicate model names followed by information on BC and domain size, namely, (L_x/L_z/BC) for finite-difference method/finite-element method (FDM/FEM), and (L_z/BC) or (half-space [HS]) for boundary element method (BEM). BC1 and BC2 refer to the far-field free surface or displacement BC and BC3 refers to the periodic BC. The color version of this figure is available only in the electronic edition.

however, illustrate how this discrepancy decreases with increased physical domain size, suggesting convergence of results across the modeling groups. Figure 5c,d shows comparisons of all models with $L_z > 160$ km, further illustrating that excellent agreements between model results can be achieved with sufficiently large domain sizes.

Although computational domain size and BCs can lead to model divergence over the long term, the coseismic behavior of individual earthquake is qualitatively well reproduced by all models. In Figure 6, we show the time series of shear stress evolution near the nucleation depth (12.5 km) and slip rate (at a midseismogenic depth of 7.5 km) during the coseismic phase for the eighth event in the sequence from Figure 5. We chose these plotting depths as they best illustrate model discrepancies, with time series aligned relative to the rupture initiation time at the depth of 12.5 km. Peak values in slip rates at 7.5 km depth occur approximately 10 s later, and coseismic surface reflection phases are marked for all four plots with black arrows. Figure 6a,b shows results from models on relatively small computational domains, revealing discrepancies in prerupture stress levels near the locked-creeping transition due to differences in interseismic loading, and resultant coseismic rupture behavior, including peak shear stress and rupture speeds as evidenced by rupture initiation times of the direct and surface-reflection phases at depth of 7.5 km. Figure 6c, d illustrate excellent agreements for model results on larger domains. The discrepancy of <1 MPa in prestress levels at transitional depths does not result in pronounced difference in fault-slip rate evolution.

Results from BP2

For BP2, we suggested submissions of multiple models with different spatial resolutions from each group (see Table 2). By design, models with a cell size that does not resolve critical length scales—process zone size and nucleation zone size defined in equations (4) and (5)—would produce increased complexity in earthquake sequences, observed previously (Rice, 1993; Ben-Zion and Rice, 1997; Day *et al.*, 2005; Lapusta and Liu, 2009), and illustrated in the cumulative slip profiles in Figure 3b–d.

Although drastic differences in small event patterns arise for large cell sizes, we found that with increasing resolution results

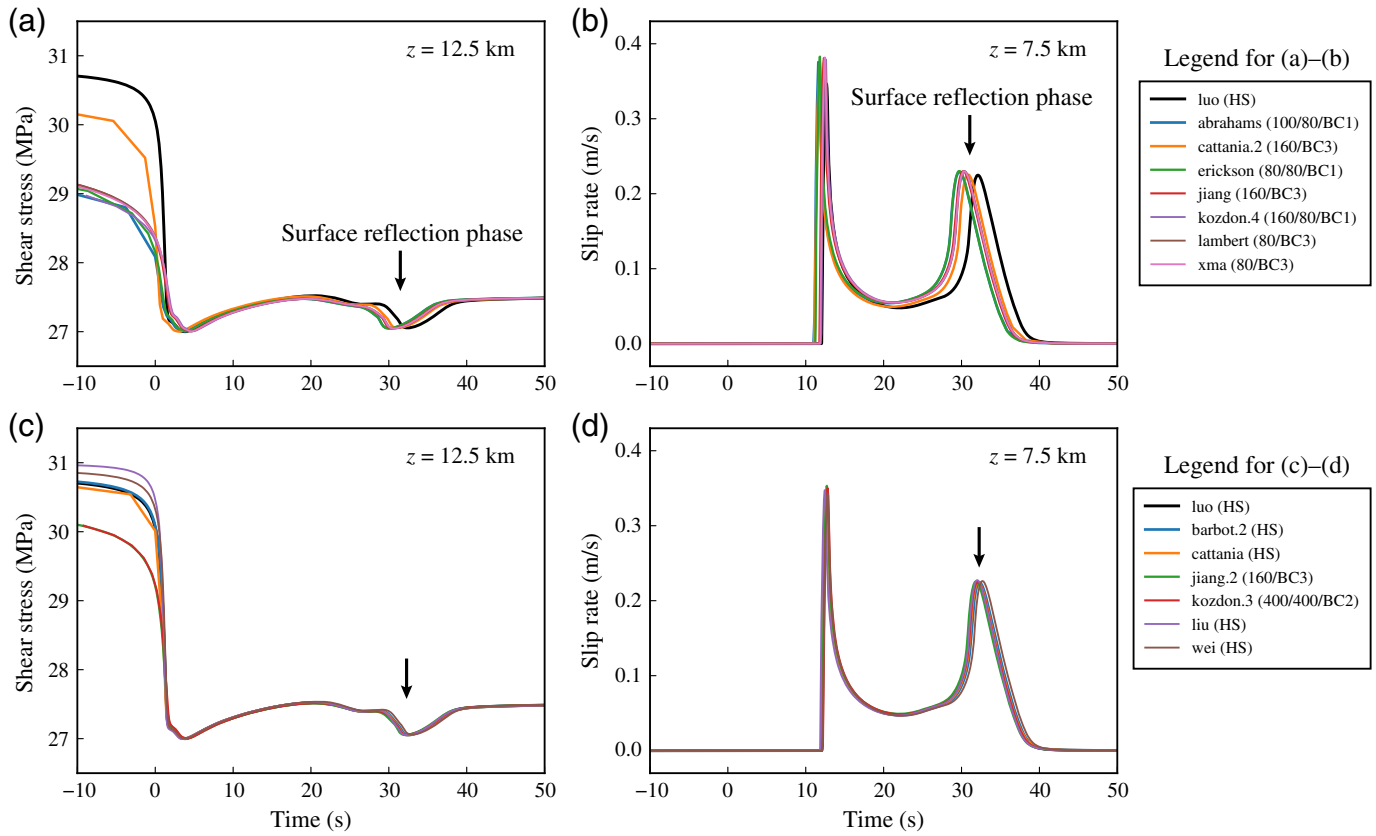

Figure 6. Coseismic behavior of BP1 models. Coseismic phase during the eighth event in Figure 5 is shown. Models with smaller computational domain sizes show discrepancies in (a) shear stresses at 12.5 km depth and (b) slip rates at 7.5 km depth. Models with sufficiently large computational domain sizes are compared for (c) shear stresses at 12.5 km depth and (d) slip rates at 7.5 km depth. Time series are aligned relative to the rupture initiation time at the depth of 12.5 km in each model. Note that the half-space solution luo is the same in (b) and (d) and serves as a reference. The surface reflection phase is marked by a black arrow. The color version of this figure is available only in the electronic edition.

converge to an alternating sequence of large and small events among most models. Figure 7a shows the long-term evolution of slip rates at 9.6 km (near the bottom of the seismogenic zone and above the earthquake initiation depth) for the best model results (with a cell size of 25 m and large computational domain sizes). We found that even models with similar cell and domain sizes tend to produce results that are initially closely matching, but diverge over time. This divergence is likely due to differences in computational techniques and/or accumulation of numerical round-off errors (or, in other words, the fact that numerical solutions to the governing equations are sensitive to finite-precision arithmetic, e.g., codes that consider a volume discretization require solving a large linear system at each timestep). However, if we zoom in on the tenth event in the sequence (gray bar in Fig. 7a), the time series of fault-slip rates, aligned with respect to the start time of seismic slip at the depth of 12 km within each model, show good agreements (Fig. 7b). Although small discrepancies exist in peak slip rates and early source complexity, partly due to differences in interevent times, the models with the highest resolution exhibit good agreements in their overall coseismic behavior despite their divergence in the long term.

Figure 8 illustrates how model agreement is gradually lost with decreased model resolution. For cell sizes of 25 and 50 m, long-term stress evolution near the locked-creeping transition is qualitatively similar for the three models shown and the offset in the timing of earthquakes does not significantly affect coseismic behavior of major events, as indicated by comparable coseismic stress drops. For large cell sizes of 100 and 200 m, not only is the time offset more random, but also coseismic stress drops and event patterns vary between models. Numerical artifacts and different computational techniques likely contribute to the divergence of simulation results.

In Figure 9, we plot the distribution of earthquake sizes, seismic moment release, and frequency-size relation for two groups of models (jiang and cattania) with increasing cell sizes. For the 2D problem, we define earthquake size as moment release per length for each event $M = \int \mu s dz$, in which shear modulus $\mu = c_s^2 \rho \approx 32$ GPa and s is the total coseismic slip over the cell. Although better resolved models (cell sizes of 25 and 50 m) show excellent agreements between the two

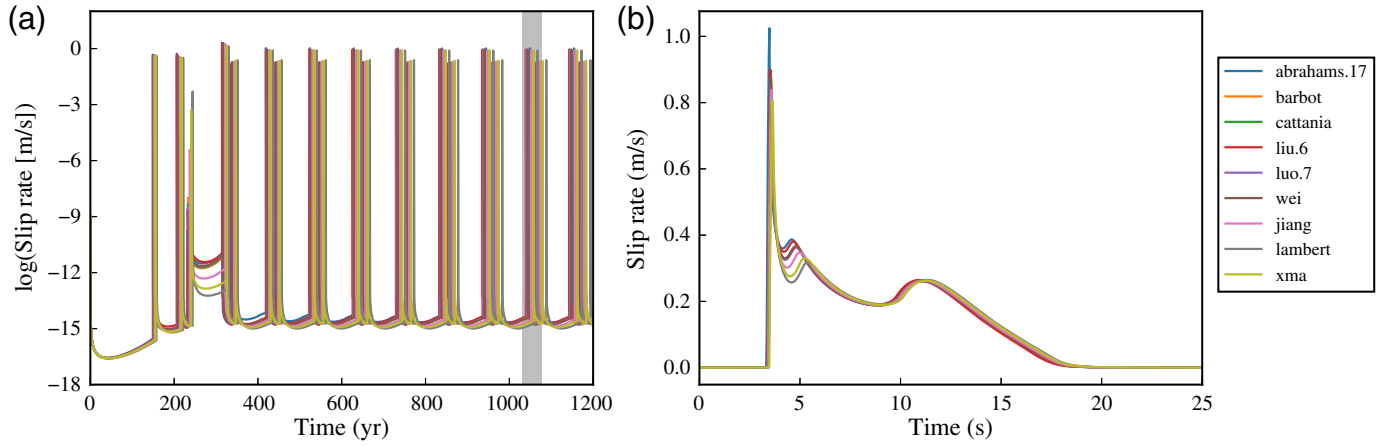

Figure 7. Comparison of best-resolved BP2 models (cell size of ~25 m). (a) Long-term evolution of slip rates at depth of 9.6 km, and (b) coseismic evolution of slip rates at the depth of 9.6 km for the tenth large events in the sequence (marked in gray in a). Time series are aligned relative to the rupture initiation time at the depth of 12 km in each model. The color version of this figure is available only in the electronic edition.

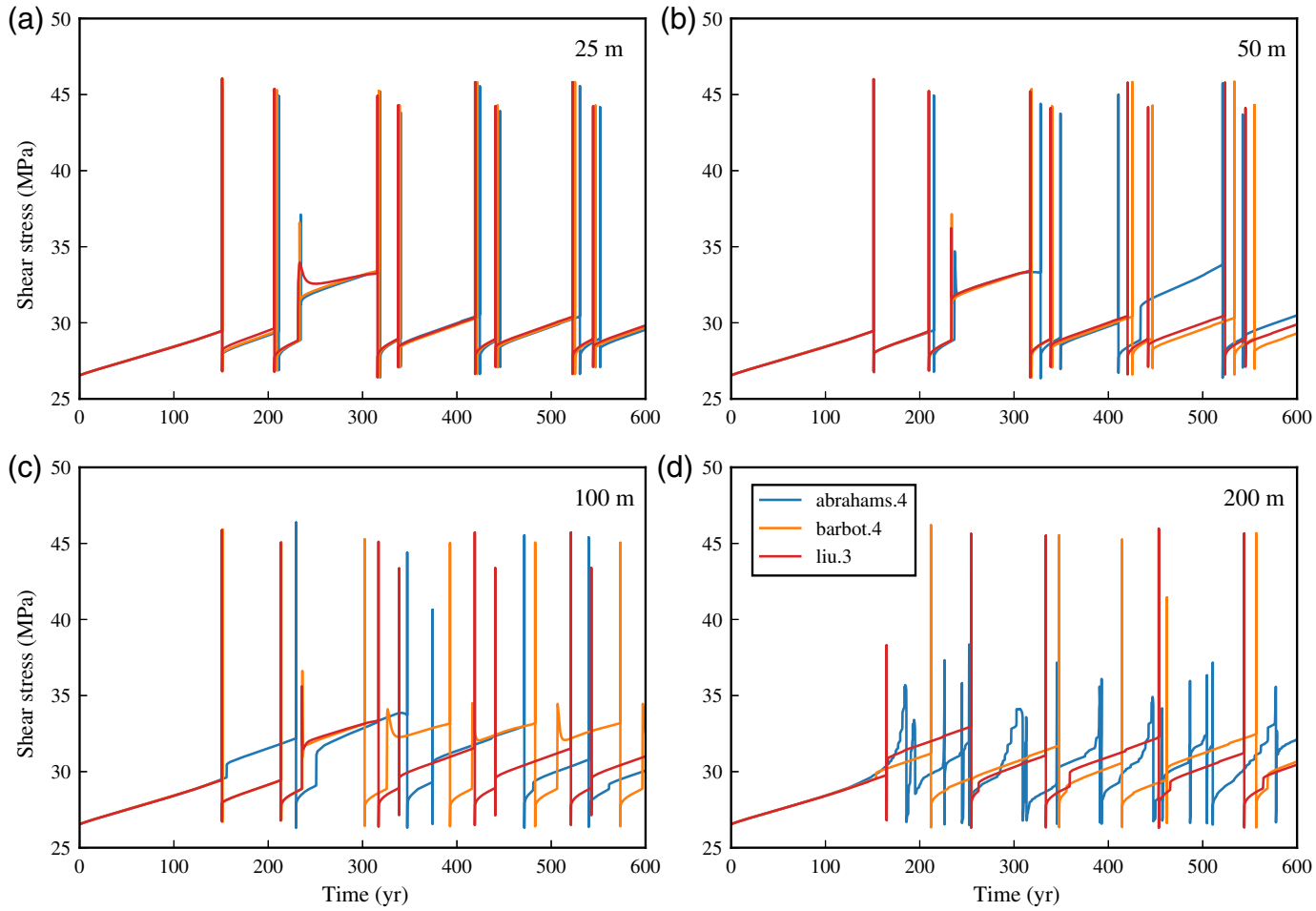

Figure 8. Increasing discrepancy in BP2 models due to an increased cell size of (a) 25, (b) 50, (c) 100, and (d) 200 m. Time evolution of shear stress at the depth of 9.6 km during the first 600 yr is shown for models from three groups (abrahams, barbot, and liu). The color version of this figure is available only in the electronic edition.

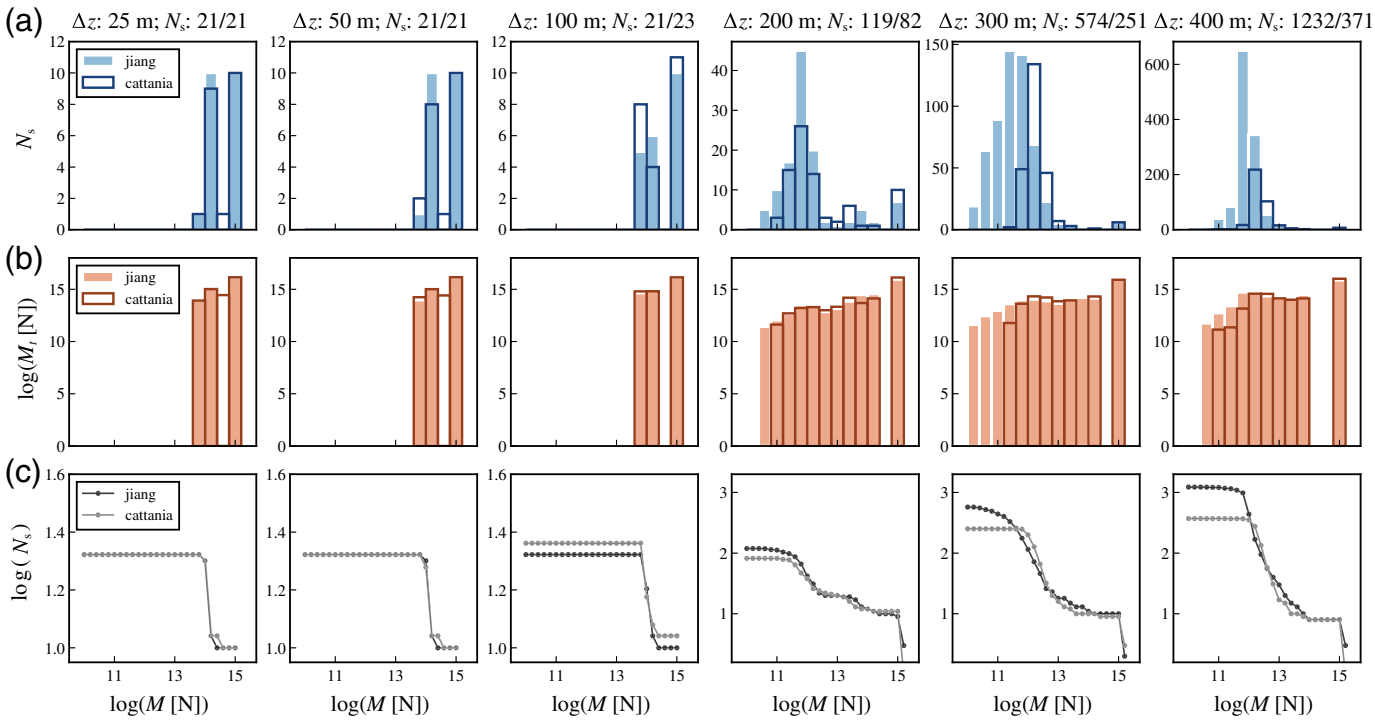

Figure 9. Effect of model resolution on earthquake patterns. Distribution of (a) earthquake sizes and of (b) total seismic moment release per unit length M (in unit of N) and (c) frequency-size relation. Models from two groups (jiang and cattania) are compared. The corresponding cell size (Δz) and total seismic event numbers (N_s) are marked in the titles. Seismic moment M refers to the seismic moment of each earthquake; total seismic moment M_t refers to the sum of moment release for all earthquakes within each magnitude bin. N_s in (c) refers to the number of seismic events with moment above the corresponding M. The color version of this figure is available only in the electronic edition.

groups, models produce dramatically different earthquake statistics when cell size increases to 400 m, with the most significant discrepancies in smaller earthquakes between the two models (Fig. 9a). The distribution of total seismic moment release M_t calculated as the sum of moment release during all earthquakes within a certain magnitude range, also changes with cell sizes, although in a similar manner for the two model groups (Fig. 9b). Overall, models with larger cell sizes tend to produce large earthquakes with reduced total moment; part of the moment deficit is accommodated through many smaller earthquakes and the rest through additional aseismic slip. For example, the total moment release through largest earthquakes in 400 m models is only half of that in 25 m models. These results demonstrate that simulated small earthquakes are especially sensitive to model resolution and large earthquake behavior can also be affected. In addition, Figure 9c reveals how different simulations with poor resolution can produce similar power-law features in frequency-size distributions over certain ranges of earthquake sizes, as a result of numerical artifacts rather than well-resolved physics.

In Figure 10, we illustrate the effect of model resolution on the partition between seismic and aseismic slip. Normalized seismic moment release R_s is plotted against depth for several modeling groups, in solid lines for total seismic moment release and dashed lines for seismic moment due to surface-breaching events. $R_s = 0$ implies that all plate motion is accommodated by aseismic slip on the fault, whereas $R_s = 1$ means that all moment is released through earthquakes. A transitional zone in this partitioning around $z = H$ and down to $z = H + h$ ($H = 15$ and $h = 3$ in this exercise) is evidenced in the well-resolved models ($\Delta z = 25$, 50, 100 m). The poorly resolved models, however, illustrate model discrepancies in the seismic and aseismic partitioning, with the near-surface slip budget being increasingly accommodated by small earthquakes and aseismic slip with increased cell sizes.

In Figure 11, we show interevent times for large surface-breaching events for all models and cell sizes, showing a strong agreement of ~110 yr for a cell size of 25 m, with an increasing variability and discrepancies among models with increased cell size. Although the range of earthquake recurrence intervals is highly dependent on cell sizes, the median values across models with larger cell sizes do not significantly deviate from the uniform recurrence intervals in well-resolved models. This suggests that at least some observables in these models retain information of the true behavior of physical models and the larger cell sizes can be viewed as a factor that leads to increased modeling errors.

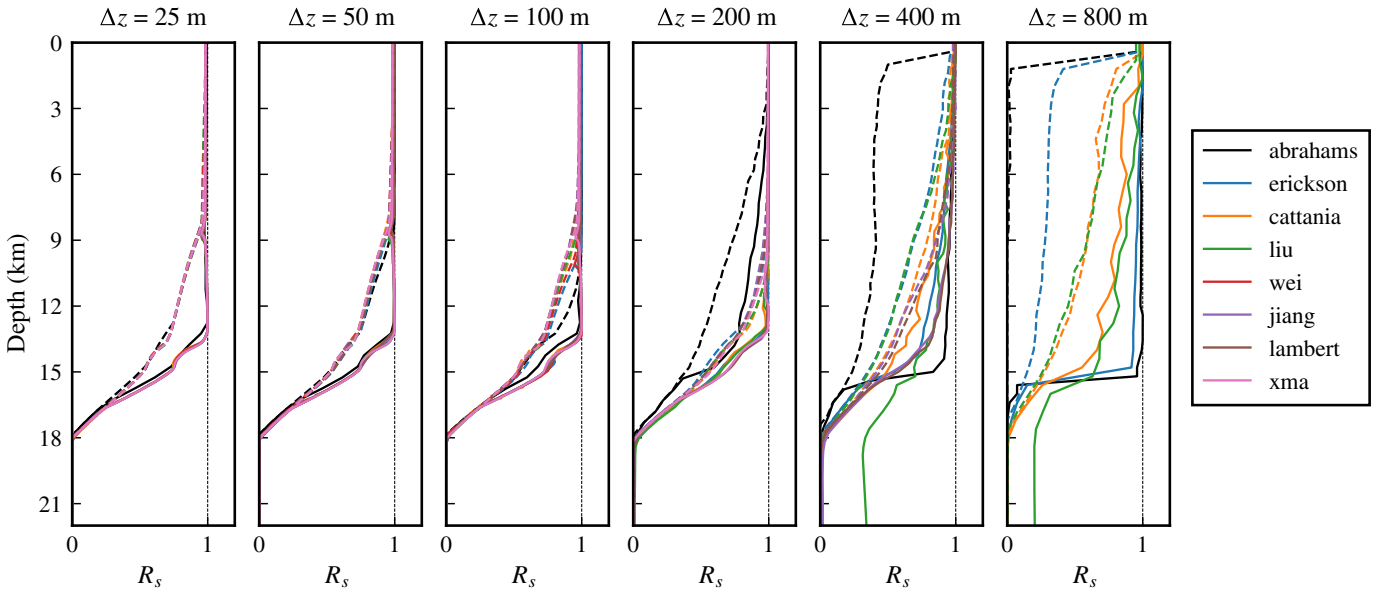

Figure 10. Effect of model resolution on seismic–aseismic slip partitioning over depth. Depth distribution of the ratio of total seismic moment release to total moment release R_s is shown by solid lines. The ratio between seismic moment due to surface-breaching earthquakes (with surface slip greater than 0.1 m) to total moment release is indicated by dashed lines. Simulations with different resolutions are shown with the same color for each modeling group. Note that not all groups have simulation results for all resolutions. The color version of this figure is available only in the electronic edition.

Conclusions and Perspectives

For the first two SEAS benchmarks, we found that discrepancies among well-resolved models were significantly influenced by computational domain size, with larger domains yielding improvements in agreements, regardless of domain BCs. Spin-up periods (time required for system to be independent of initial conditions) for well-resolved models was relatively short—approximately 2–3 events. Results on large domains agree well initially but still diverge over time, which was not unexpected due to accumulation of round-off errors (sensitivity to finite-precision arithmetic) and differences in computational techniques. Future benchmark exercises will need to contend with the issue of model divergence, particularly when physical complexities and nonlinear dynamics mean that event sequences are not periodic. Our future work involves designing SEAS-appropriate metrics (as was done for dynamic rupture comparisons in Barall and Harris, 2015), for example, comparisons of event statistics such as frequency–magnitude distributions.

For BP2, we investigated model resolution and observed qualitative similarities of bimodal events when the process zone was resolved by approximately three and six grid points, suggesting model convergence. A failure to resolve this length scale, however, can lead to substantial differences in long-term fault behavior as well as earthquake statistics relevant to seismic hazard such as frequency-size distributions and interevent times.

Although our initial benchmarks have a simple setup, comparison of results for tens of models have yielded some unexpected and important insights, affirming the importance of starting simple in a community code verification exercise. The results and lessons from our initial benchmarks prepare us for future benchmark problems that incrementally incorporate additional, potentially dominating physical factors, including fully dynamic ruptures, coupling with fluids, multiple fault segments, nonplanar fault geometries, and inelastic bulk constitutive behavior (e.g., Segall and Rice, 1995, 2006; Noda and Lapusta, 2010; Segall *et al.*, 2010; Lambert and Barbot, 2016; Qiu *et al.*, 2016; Erickson *et al.*, 2017; Barbot, 2018; Ong *et al.*, 2019). For future verification exercises, we plan to address important issues in SEAS simulations such as 3D effects, heterogeneous fault frictional properties, and full dynamics, which should advance the state-of-the-art computational capabilities in our field.

One of the main purposes of code comparison studies is to promote confidence in model outcomes when exact solutions to the underlying physical problems are not known (which is often the case when physical and geometrical complexities are present). To this end, code comparisons are one important technique to verify model outcomes. However, individual convergence tests can also be done either through self-convergence tests (e.g., by computing a reference numerical solution obtained with high-mesh resolution and order of accuracy as done in Wollherr *et al.*, 2018, or using several mesh refinements to estimate a convergence rate as done in Kozdon *et al.*, 2019) or through the method of manufactured solutions (MMS) (Roache, 1998). One potential downside of the self-convergence technique is that it may not recognize errors made

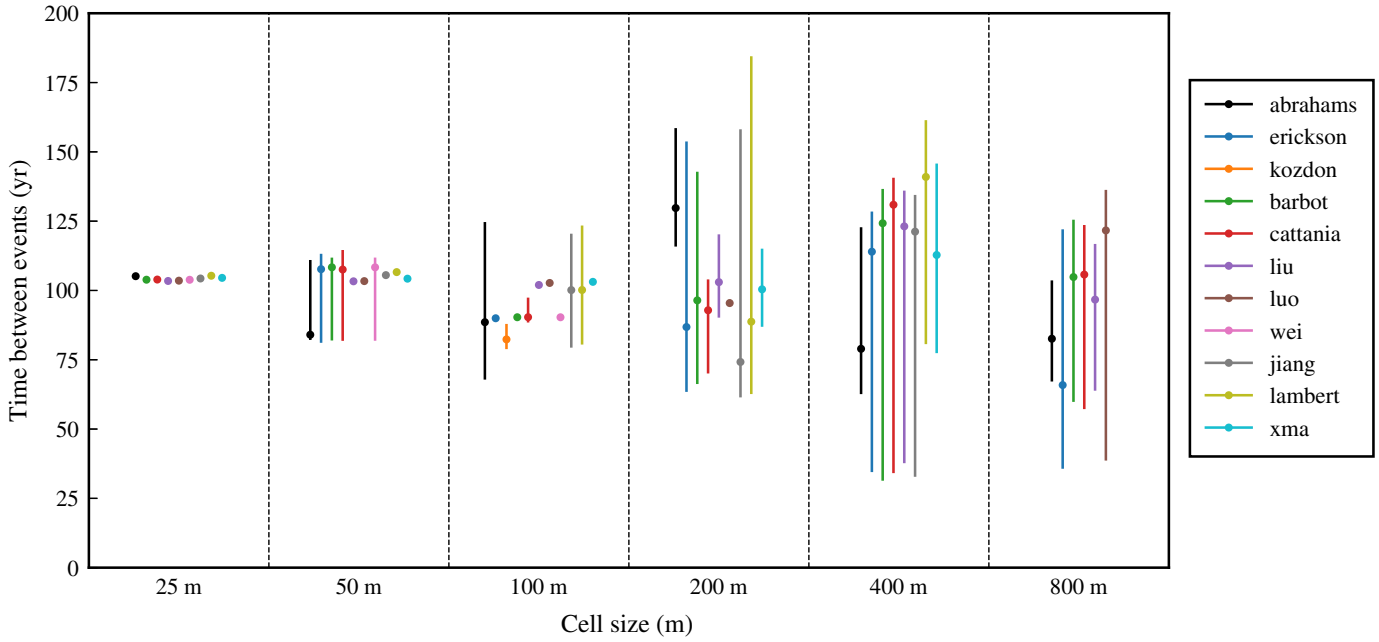

Figure 11. Effect of model resolution on recurrence intervals of large surface-breaching events. The vertical lines indicate the range of recurrence interval values, with the median value marked as dots. The color version of this figure is available only in the electronic edition.

in the discretization of the governing partial differential equations (PDEs) and may ascertain convergence toward a solution to an incorrect problem. The MMS technique, on the other hand, obtains an analytic solution to the underlying governing equation by modifying its prescribed data (e.g., by adding a source term to the PDE). These exact solutions can be manufactured even with nonlinearities and complex geometries present, allowing for rigorous convergence tests toward a known solution (e.g., Kozdon and Dunham, 2013; Erickson and Dunham, 2014). A drawback of MMS, however, is that the technique often changes important length and time scales present in the problem, so that the manufactured solution does not exhibit physical quantities of interest for the application in mind. Code comparison studies provide an alternative route. For example, in SEAS models, we want some assurance that our codes are producing earthquake recurrence times and magnitudes that are reasonably correct (robust against choice of numerical methods), particularly when using cell sizes at the limit of computational feasibility, which can be verified through code comparisons studies.

The goal of the SEAS initiative is to promote advanced models with robust physical features—a large spectrum of rupture styles and patterns, including slow-slip events, complex earthquake sequences, fluid effects, dynamic stress changes, and inelastic deformation—that are currently missing in the large-scale, long-term earthquake simulator frameworks such as viscoelastic earthquake simulator, Rate-State earthQuake Simulator, Virtual California, and ALL California fault model (Pollitz, 2012; Richards-Dinger and Dieterich, 2012; Sachs *et al.*, 2012; Ward, 2012). This new generation of verified SEAS models will help determine the controlling physical mechanisms of earthquake nucleation, propagation, and arrest. The community-wide initiative would also provide incentives and new ideas to characterize modeling uncertainty for the increasingly complex earthquake source models, an important step in using physics-based models for the assessment of seismic hazard. Future validation efforts comparing physics-based models with geophysical observations will bridge studies in paleoseismology, geodesy, and seismology to understand fault behavior over multiple temporal and spatial scales.

Data and Resources

Our online platform (http://scecdata.usc.edu/cvws/seas/) is being developed and maintained by Michael Barall. The data for local fault properties are stored on the platform. Full details of the benchmark including governing equations and initial and fault interface conditions are available at http://scecdata.usc.edu/cvws/seas/index.html. Southern California Earthquake Center (SCEC) funded workshop presentations are available at http://scecdata.usc.edu/cvws/seas/workshop_presentations.html. SCycle code is available at https://github.com/kali-allison/SCycle. FDCycle code is available at https://github.com/brittany-erickson/FDCycle. QDESDG code is available at https://github.com/jkozdon/QDESDG. Quasi-DYNamic earthquake simulator (QDYN) code is available at https://github.com/ydluo/qdyn. All websites were last accessed in December 2019.

Acknowledgments

The authors thank Steve Day, Alice-Agnes Gabriel, Jeff McGuire, and Fred Pollitz for reviewing the article. Brittany A. Erickson, Junle Jiang, and Michael Barall were supported through the Southern California

Earthquake Center Grant Numbers 18099 and 19109. Two sequences of earthquakes and aseismic slip (SEAS)-themed workshops were funded by Southern California Earthquake Center (SCEC) Award Numbers 17151 and 18102. SCEC is funded by National Science Foundation (NSF) Cooperative Agreement EAR-0529922 and U.S. Geological Survey (USGS) Cooperative Agreement 07HQAG0008. This is SCEC Contribution Number 9066. Brittany A. Erickson and Junle Jiang designed the benchmark problems, analyzed model results, co-organized the workshops and cowrote this article, with equal contributions. Michael Barall developed and maintains the online platform. Michael Barall, Nadia Lapusta, Eric M. Dunham, and Ruth Harris provided major support and advice in forming the working group, obtaining funding, and manuscript writing. Remaining coauthors provided feedback on benchmark designs, participated in the benchmark exercises, helped revise the article and are hence listed alphabetically.

Any use of trade, firm, or product names is for descriptive purposes only and does not imply endorsement by the U.S. Government.

References

Abdelmeguid, M., X. Ma, and A. Elbanna (2019). A novel hybrid finite element-spectral boundary integral scheme for modeling earthquake cycles: Application to rate and state faults with low-velocity zones, *J. Geophys. Res.* doi: 10.31223/osf.io/xwhbs.

Allison, K., and E. M. Dunham (2018). Earthquake cycle simulations with rate-and-state friction and power-law viscoelasticity, *Tectonophysics* **733,** 232–256, doi: 10.1016/j.tecto.2017.10.021.

Ampuero, J.-P., and A. M. Rubin (2008). Earthquake nucleation on rate and state faults—Aging and slip laws, *J. Geophys. Res.* **113,** no. B1, doi: 10.1029/2007JB005082.

Andrews, D. J. (1976a). Rupture propagation with finite stress in antiplane strain, *J. Geophys. Res.* **81,** 3575–3582.

Andrews, D. J. (1976b). Rupture velocity of plane strain shear cracks, *J. Geophys. Res.* **81,** 5679–5687.

Aochi, H., and C. Twardzik (2019). Imaging of seismogenic asperities of the 2016 ML 6.0 Amatrice, Central Italy, earthquake through dynamic rupture simulations, *Pure Appl. Geophys.* doi: 10.1007/s00024-019-02199-z.

Barall, M., and R. A. Harris (2015). Metrics for comparing dynamic earthquake rupture simulations, *Seismol. Res. Lett.* **86,** no. 1, doi: 10.1785/0220140122.

Barbot, S. (2018). Asthenosphere flow modulated by megathrust earthquake cycles, *Geophys. Res. Lett.* **45,** 6018–6031, doi: 10.1029/2018GL078197.

Barbot, S. (2019). Slow-slip, slow earthquakes, period-two cycles, full and partial ruptures, and deterministic chaos in a single asperity fault, *Tectonophysics* doi: 10.1016/j.tecto.2019.228171.

Barbot, S., Y. Fialko, and Y. Bock (2009). Postseismic deformation due to the Mw 6.0 2004 Parkfield earthquake: Stress-driven creep on a fault with spatially variable rate-and-state friction parameters, *J. Geophys. Res.* **114,** no. B07405, doi: 10.1029/2008JB005748.

Barbot, S., N. Lapusta, and J.-P. Avouac (2012). Under the hood of the earthquake machine: Toward predictive modeling of the seismic cycle, *Science* **336,** no. 6082, 707–710, doi: 10.1126/science.1218796.

Ben-Zion, Y., and J. R. Rice (1997). Dynamic simulations of slip on a smooth fault in an elastic solid, *J. Geophys. Res.* **102,** no. B8, 17,771–17,784, doi: 10.1029/97JB01341.

Bhat, H. S., M. Olives, R. Dmowska, and J. R. Rice (2007). Role of fault branches in earthquake rupture dynamics, *J. Geophys. Res.* **112,** no. B11309, 16, doi: 10.1029/2007JB005027.

Blanpied, M. L., D. A. Lockner, and J. D. Byerlee (1991). Fault stability inferred from granite sliding experiments at hydrothermal conditions, *Geophys. Res. Lett.* **18,** no. 4, 609–612.

Bradley, A. M. (2014). Software for efficient static dislocation-traction calculations in fault simulators, *Seismol. Res. Lett.* **85,** no. 6, 1358–1365, doi: 10.1785/0220140092.

Cattania, C. (2019). Complex earthquake behavior on simple faults, *Geophys. Res. Lett.* doi: 10.31223/osf.io/hgbjx.

Chen, T., and N. Lapusta (2009). Scaling of small repeating earthquakes explained by interaction of seismic and aseismic slip in a rate and state fault model, *J. Geophys. Res.* **114,** no. B01311, doi: 10.1029/2008JB005749.

Christensen, N. I. (1989). *Seismic Properties of Rocks*, Van Nostrand Reinhold and Company, New York, New York, 1093–1098.

Day, S. M. (1982). Three-dimensional finite difference simulation of fault dynamics: Rectangular faults with fixed rupture velocity, *Bull. Seismol. Soc. Am.* **72,** no. 3, 705–727.

Day, S. M., L. A. Dalguer, N. Lapusta, and Y. Liu (2005). Comparison of finite difference and boundary integral solutions to three-dimensional spontaneous rupture, *J. Geophys. Res.* **110,** no. B12, doi: 10.1029/2005JB003813.

Dieterich, J. H. (1979). Modeling of rock friction: 1. Experimental results and constitutive equations, *J. Geophys. Res.* **84,** no. B5, 2161–2168, doi: 10.1029/JB084iB05p02161.

Dieterich, J. H., K. B. Richards-Dinger, and K. A. Kroll (2015). Modeling injection-induced seismicity with the physics-based earthquake simulator RSQSim, *Seismol. Res. Lett.* **86,** no. 4, doi: 10.1785/0220150057.

Duan, B., and D. D. Oglesby (2006). Heterogeneous fault stresses from previous earthquakes and the effect on dynamics of parallel strike-slip faults, *J. Geophys. Res.* **111,** no. B5, 1–15, doi: 10.1029/2005JB004138.

Dublanchet, P. (2017). The dynamics of earthquake precursors controlled by effective friction, *Geophys. J. Int.* **212,** no. 2, 853–871.

Dublanchet, P., P. Bernard, and P. Favreau (2013). Interactions and triggering in a 3-d rate-and-state asperity model, *J. Geophys. Res.* **118,** no. 5, 2225–2245.

Dunham, E. M., D. Belanger, L. Cong, and J. E. Kozdon (2011a). Earthquake ruptures with strongly rate-weakening friction and off-fault plasticity, Part:1: Planar faults, *Bull. Seismol. Soc. Am.* **101,** no. 5, 2296–2307, doi: 10.1785/0120100075.

Dunham, E. M., D. Belanger, L. Cong, and J. E. Kozdon (2011b). Earthquake ruptures with strongly rate-weakening friction and off-fault plasticity, Part:2: Nonplanar faults, *Bull. Seismol. Soc. Am.* **101,** no. 5, 2308–2322, doi: 10.1785/0120100076.

Erickson, B. A., and E. M. Dunham (2014). An efficient numerical method for earthquake cycles in heterogeneous media: Alternating subbasin and surface-rupturing events on faults crossing a sedimentary basin, *J. Geophys. Res.* **119,** no. 4, 3290–3316, doi: 10.1002/2013JB010614.

Erickson, B. A., E. M. Dunham, and A. Khosravifar (2017). A finite difference method for off-fault plasticity throughout the earthquake cycle, *J. Mech. Phys. Solid.* **109,** 50–77, doi: 10.1016/j.jmps.2017.08.002.

Floyd, M. A., R. J. Walters, J. R. Elliott, G. J. Funning, J. L. Svarc, J. R. Murray, A. J. Hooper, Y. Larsen, P. Marinkovic, R. Bürgmann, *et al.*

(2016). Spatial variations in fault friction related to lithology from rupture and afterslip of the 2014 South Napa, California, earthquake, *Geophys. Res. Lett.* **43,** no. 13, 6808–6816, doi: 10.1002/2016GL069428.

Gabriel, A.-A., J.-P. Ampuero, L. A. Dalguer, and P. M. Mai (2012). The transition of dynamic rupture styles in elastic media under velocity-weakening friction, *J. Geophys. Res.* **117,** no. B9, 1–20, doi: 10.1029/2012JB009468.

Gallovic, F., L. Valentova, J.-P. Ampuero, and A.-A. Gabriel (2019). Bayesian dynamic finite-fault inversion: 1. Method and synthetic test, *J. Geophys. Res.* **124,** no. 7, 6949–6969, doi: 10.1029/2019JB017510.

Goswami, A., and S. Barbot (2018). Slow-slip events in semi-brittle serpentinite fault zones, *Sci. Rept.* **8,** no. 1, 6181.

Harris, R. A., M. Barall, B. Aagaard, S. Ma, D. Roten, K. Olsen, B. Duan, D. Liu, B. Luo, K. Bai, *et al.* (2018). A suite of exercises for verifying dynamic earthquake rupture codes, *Seismol. Res. Lett.* **89,** no. 3, doi: 10.1785/0220170222.

Harris, R. A., M. Barall, R. Archuleta, E. Dunham, B. Aagaard, J. P. Ampuero, H. Bhat, V. Cruz-Atienza, L. Dalguer, P. Dawson, *et al.* (2009). The SCEC/USGS dynamic earthquake rupture code verification exercise, *Seismol. Res. Lett.* **80,** 119–126, doi: 10.1785/gssrl.80.1.119.

Hori, T., N. Kato, K. Hirahara, T. Baba, and Y. Kaneda (2004). A numerical simulation of earthquake cycles along the Nankai Trough in southwest Japan: Lateral variation in frictional property due to the slab geometry controls the nucleation position, *Earth Planet Sci. Lett.* **228,** nos. 3/4, 215–226.

Jiang, J., and Y. Fialko (2016). Reconciling seismicity and geodetic locking depths on the Anza section of the San Jacinto fault, *Geophys. Res. Lett.* **43,** no. 20, 10,663–10,671, doi: 10.1002/2016GL071113.

Jiang, J., and N. Lapusta (2016). Deeper penetration of large earthquakes on seismically quiescent faults, *Science* **352,** no. 6291, 1293–1297, doi: 10.1126/science.aaf1496.

Johnson, K. M., R. Bürgmann, and K. Larson (2006). Frictional properties of the San Andreas Fault near Parkfield, California, inferred from models of afterslip following the 2004 earthquake, *Bull. Seismol. Soc. Am.* **96,** no. 4B, doi: 10.1785/0120050808.

Kaneko, Y., J.-P. Ampuero, and N. Lapusta (2011). Spectral-element simulations of long-term fault slip: Effect of low-rigidity layers on earthquake-cycle dynamics, *J. Geophys. Res.* **116,** no. B10, doi: 10.1029/2011JB008395.

Kaneko, Y., J.-P. Avouac, and N. Lapusta (2010). Towards inferring earthquake patterns from geodetic observations of interseismic coupling, *Nature Geosci.* **3,** 363–369, doi: 10.1038/ngeo843.

Kato, N. (2002). Seismic cycle on a strike-slip fault with rate-and state-dependent strength in an elastic layer overlying a viscoelastic half-space, *Earth Planets Space* **54,** no. 11, 1077–1083.

Kato, N. (2014). Deterministic chaos in a simulated sequence of slip events on a single isolated asperity, *Geophys. J. Int.* **198,** no. 2, 727–736.

Kato, N. (2016). Earthquake cycles in a model of interacting fault patches: Complex behavior at transition from seismic to aseismic slip, *Bull. Seismol. Soc. Am.* **106,** no. 4, 1772–1787.

Kozdon, J. E., and E. M. Dunham (2013). Rupture to the trench: Dynamic rupture simulations of the 11 March 2011 Tohoku earthquake, *Bull. Seismol. Soc. Am.* **103,** no. 2B, 1275–1289, doi: 10.1785/0120120136.

Kozdon, J. E., L. C. Wilcox, T. Hagstrom, and J. W. Banks (2019). Robust approaches to handling complex geometries with Galerkin difference methods, *J. Comput. Phys.* **392,** 483–510, doi: 10.1016/j.jcp.2019.04.031.

Lambert, V., and S. Barbot (2016). Contribution of viscoelastic flow in earthquake cycles within the lithosphere-asthenosphere system, *Geophys. Res. Lett.* **43,** no. 19, 142–154.

Lapusta, N., and Y. Liu (2009). Three-dimensional boundary integral modeling of spontaneous earthquake sequences and aseismic slip, *J. Geophys. Res.* **114,** no. B9, doi: 10.1029/2008JB005934.

Lapusta, N., and J. R. Rice (2003). Nucleation and early seismic propagation of small and large events in a crustal earthquake model, *J. Geophys. Res.* **108,** no. B4, 2205.

Lapusta, N., J. R. Rice, Y. Ben-Zion, and G. Zheng (2000). Elastodynamic analysis for slow tectonic loading with spontaneous rupture episodes on faults with rate- and state-dependent friction, *J. Geophys. Res.* **105,** no. B10, 23,765–23,789, doi: 10.1029/2000JB900250.

Li, D., and Y. Liu (2016). Spatiotemporal evolution of slow slip events in a nonplanar fault model for northern Cascadia subduction zone, *J. Geophys. Res.* **121,** no. 9, 6828–6845.

Li, D., and Y. Liu (2017). Modeling slow-slip segmentation in Cascadia subduction zone constrained by tremor locations and gravity anomalies, *J. Geophys. Res.* **122,** no. 4, 3138–3157.

Liu, Y. (2013). Numerical simulations on megathrust rupture stabilized under strong dilatancy strengthening in slow slip region, *Geophys. Res. Lett.* **40,** no. 7, 1311–1316, doi: 10.1002/grl.50298.

Liu, Y., and J. R. Rice (2005). Aseismic slip transients emerge spontaneously in three-dimensional rate and state modeling of subduction earthquake sequences, *J. Geophys. Res.* **110,** no. B08307, doi: 10.1029/2004JB003424.

Liu, Y., and J. R. Rice (2007). Spontaneous and triggered aseismic deformation transients in a subduction fault model, *J. Geophys. Res.* **112,** no. B09404, doi: 10.1029/2007JB004930.

Lozos, J. C., D. D. Oglesby, B. Duan, and S. G. Wesnousky (2011). The effects of double fault bends on rupture propagation: A geometrical parameter study, *Bull. Seismol. Soc. Am.* **101,** no. 1, 385–398.

Luo, Y., and J. P. Ampuero (2011). Numerical simulation of tremor migration triggered by slow slip and rapid tremor reversals, *AGU Fall Meeting Abstracts, S33C–02*, San Francisco, California, 5–9 December 2011.

Luo, Y., and J. P. Ampuero (2017). Preprint: Tremor migration patterns and the collective behavior of deep asperities mediated by creep, *EarthArXiv*, doi: 10.31223/osf.io/mbcav.

Ma, S., and D. J. Andrews (2010). Inelastic off-fault response and three-dimensional earthquake rupture dynamics on a strike-slip fault, *J. Geophys. Res.* **115,** no. B04304, doi: 10.1029/2009JB006382.

Ma, X., and A. Elbanna (2019). Dynamic rupture propagation on fault planes with explicit representation of short branches, *Earth Planet Sci. Lett.* **523,** 115702, doi: 10.1016/j.epsl.2019.07.005.

Marone, C. (1998). Laboratory-derived friction laws and their application to seismic faulting, *Annu. Rev. Earth Planet. Sci.* **26,** no. 1, 643–696, doi: 10.1146/annurev.earth.26.1.643.

McClure, M. W., and R. N. Horne (2011). Investigation of injection-induced seismicity using a coupled fluid flow and rate/state friction model, *Geophysics* **76,** no. 6, WC181–WC198, doi: 10.1190/geo2011-0064.1.

Mckay, M. B., B. A. Erickson, and J. E. Kozdon (2019). A computational method for earthquake cycles within anisotropic media, *Geophys. J. Int.* doi: 10.1093/gji/ggz320.

Meade, B. J., Y. Klinger, and E. A. Hetland (2013). Inference of multiple earthquake-cycle relaxation timescales from irregular geodetic sampling of interseismic deformation, *Bull. Seismol. Soc. Am.* **103,** no. 5, 2824–2835, doi: 10.1785/0120130006.

Mele Veedu, M., and S. Barbot (2016). The Parkfield tremors reveal slow and fast ruptures on the same asperity, *Nature* **532,** no. 7599, 361–365, doi: 10.1038/nature17190.

Michel, S., J.-P. Avouac, N. Lapusta, and J. Jiang (2017). Pulse-like partial ruptures and high-frequency radiation at creeping-locked transition during megathrust earthquakes, *Geophys. Res. Lett.* **44,** no. 16, 8345–8351, doi: 10.1002/2017GL074725.

Mitsui, Y., and K. Hirahara (2011). Fault instability on a finite and planar fault related to early phase of nucleation, *J. Geophys. Res.* **116,** no. B6, 1–14, doi: 10.1029/2010JB007974.

Nakata, R., M. Hyodo, and T. Hori (2012). Numerical simulation of afterslips and slow slip events that occurred in the same area in Hyuga-nada of southwest Japan, *Geophys. J. Int.* **190,** no. 2, 1213–1220, doi: 10.1111/j.1365-246X.2012.05552.x.

Nielsen, S. B., J. Carlson, and K. B. Olsen (2000). Influence of friction and fault geometry on earthquake rupture, *J. Geophys. Res.* **105,** no. B3, 6069–6088.

Noda, H., and N. Lapusta (2010). Three-dimensional earthquake sequence simulations with evolving temperature and pore pressure due to shear heating: Effect of heterogeneous hydraulic diffusivity, *J. Geophys. Res.* **115,** no. B12314, doi: 10.1029/2010JB007780.

Noda, H., and N. Lapusta (2013). Stable creeping fault segments can become destructive as a result of dynamic weakening, *Nature* **493,** no. 7433, 518–521.

Noda, H., E. M. Dunham, and J. R. Rice (2009). Earthquake ruptures with thermal weakening and the operation of major faults at low overall stress levels, *J. Geophys. Res.* **114,** no. B7, doi: 10.1029/2008JB006143.

Ohtani, M., and K. Hirahara (2015). Effect of the Earth's surface topography on quasi-dynamic earthquake cycles, *Geophys. J. Int.* **203,** no. 1, 384–398, doi: 10.1093/gji/ggv187.

Olsen, K. B., R. Madariaga, and R. J. Archuleta (1997). Three-dimensional dynamic simulation of the 1992 Landers earthquake, *Science* **278,** no. 5339, 834–838.

Ong, M. S. Q., S. Barbot, and J. Hubbard (2019). Physics-based scenario of earthquake cycles on the Ventura thrust system, California: The effect of variable friction and fault geometry, *J. Pure Appl. Geophys.* doi: 10.1007/s00024-019-02111-9.

Palmer, A. C., and J. R. Rice (1973). The growth of slip surfaces in the progressive failure of over-consolidated clay, *Proc. Math. Phys. Sci.* **332,** no. 1591, 527–548, doi: 10.1098/rspa.1973.0040.

Perfettini, H., and J.-P. Ampuero (2008). Dynamics of a velocity strengthening fault region: Implications for slow earthquakes and postseismic slip, *J. Geophys. Res.* **113,** no. B9, doi: 10.1029/2007JB005398.

Perfettini, H., and J.-P. Avouac (2004). Postseismic relaxation driven by brittle creep: A possible mechanism to reconcile geodetic measurements and the decay rate of aftershocks, application to the Chi-Chi earthquake, Taiwan, *J. Geophys. Res.* **109,** no. B02304, 1–15, doi: 10.1029/2003JB002488.

Perfettini, H., and J.-P. Avouac (2007). Modeling afterslip and aftershocks following the 1992 Landers earthquake, *J. Geophys. Res.* **112,** no. B07409, 1–19, doi: 10.1029/2006JB004399.

Pollitz, F. F. (2012). ViscoSim earthquake simulator, *Seismol. Res. Lett.* **83,** no. 6, 979–982, doi: 10.1785/0220120050.

Qiu, Q., E. M. Hill, S. Barbot, J. Hubbard, W. Feng, E. O. Lindsey, L. Feng, K. Dai, S. V. Samsonov, P. Tapponnier, *et al.* (2016). The mechanism of partial rupture of a locked megathrust: The role of fault morphology, *Geology* **44,** no. 10, 875–878, doi: 10.1130/G38178.1.

Rice, J. R. (1992). Fault stress states, pore pressure distributions, and the weakness of the San Andreas fault, in *Fault Mechanics and Transport Properties of Rocks*, B. Evans and T.-F. Wong (Editors), chap. 20, Academic Press, San Diego, California, 475–503.

Rice, J. R. (1993). Spatio-temporal complexity of slip on a fault, *J. Geophys. Res.* **98,** no. B6, 9885–9907.

Rice, J. R., and S. T. Tse (1986). Dynamic motion of a single degree of freedom system following a rate and state dependent friction law, *J. Geophys. Res.* **91,** no. B1, 521–530.

Richards-Dinger, K., and J. H. Dieterich (2012). RSQSim earthquake simulator, *Bull. Seismol. Soc. Am.* **83,** no. 6, 983–990, doi: 10.1785/0220120105.

Ripperger, J., J.-P. Ampuero, P. M. Mai, and D. Giardini (2007). Earthquake source characteristics from dynamic rupture with constrained stochastic fault stress, *J. Geophys. Res.* **112,** no. B4, doi: 10.1029/2006JB004515.

Roache, P. (1998). *Verification and Validation in Computational Science and Engineering*, First Ed., Hermosa Publishers, Albuquerque, New Mexico.

Rubin, A. M., and J.-P. Ampuero (2005). Earthquake nucleation on (aging) rate and state faults, *J. Geophys. Res.* **110,** no. B11, doi: 10.1029/2005JB003686.

Ruina, A. (1983). Slip instability and state variable friction laws, *J. Geophys. Res.* **88,** no. B12, 10,359–10,370, doi: 10.1029/JB088iB12p10359.

Sachs, M. K., E. M. Heien, D. L. Turcotte, M. B. Yikilmaz, J. B. Rundle, and L. H. Kellogg (2012). Virtual California earthquake simulator, *Seismol. Res. Lett.* **83,** no. 6, 973–978, doi: 10.1785/0220120052.

Segall, P., and A. M. Bradley (2012a). The role of thermal pressurization and dilatancy in controlling the rate of fault slip, *J. Appl. Mech.* **79,** no. 3, doi: 10.1115/1.4005896.

Segall, P., and A. M. Bradley (2012b). Slow-slip evolves into megathrust earthquakes in 2d numerical simulations, *Geophys. Res. Lett.* **39,** no. 18, doi: 10.1029/2012GL052811.

Segall, P., and J. R. Rice (1995). Dilatancy, compaction, and slip instability of a fluid infiltrated fault, *J. Geophys. Res.* **100,** 22,155–22,171.

Segall, P., and J. R. Rice (2006). Does shear heating of pore fluid contribute to earthquake nucleation?, *J. Geophys. Res.* **111,** no. B09316, 17.

Segall, P., A. M. Rubin, A. M. Bradley, and J. R. Rice (2010). Dilatant strengthening as a mechanism for slow slip events, *J. Geophys. Res.* **115,** no. B12305, 1–37, doi: 10.1029/2010JB007449.

Shi, Z., and S. M. Day (2013). Rupture dynamics and ground motion from 3-d rough-fault simulations, *J. Geophys. Res.* **118,** no. 3, 1122–1141, doi: 10.1002/jgrb.50094.

Tape, C., Q. Liu, A. Maggi, and J. Trom (2009). Adjoint tomography of the southern California crust, *Science* **325,** 988–992.

Tse, S. T., and J. R. Rice (1986). Crustal earthquake instability in relation to the depth variation of frictional slip properties, *J. Geophys. Res.* **91,** no. B9, 9452–9472.

Tullis, T. E., K. Richards-Dinger, M. Barall, J. H. Dieterich, E. H. Field, E. M. Heien, L. H. Kellogg, F. F. Pollitz, J. B. Rundle, M. K. Sachs, *et al.* (2012). Generic earthquake simulator, *Seismol. Res. Lett.* **83,** 959–963, doi: 10.1785/0220120093.

van Dinther, Y., T. V. Gerya, L. A. Dalguer, F. Corbi, F. Funiciello, and P. M. Mai (2013). The seismic cycle at subduction thrusts: 2. Dynamic implications of geodynamic simulations validated with laboratory models, *J. Geophys. Res.* **118,** no. 4, 1502–1525, doi: 10.1029/2012JB009479.

van Zelst, I., S. Wollherr, A.-A. Gabriel, E. Madden, and Y. van Dinther (2019). Modeling megathrust earthquakes across scales: One-way coupling from geodynamics and seismic cycles to dynamic rupture, *J. Geophys. Res.* **124,** 1–33, doi: 10.1029/2019JB017539.

Viesca, R. C. (2016a). Stable and unstable development of an interfacial sliding instability, *Phys. Rev. E* **93,** 060202, doi: 10.1103/PhysRevE.93.060202.

Viesca, R. C. (2016b). Self-similar slip instability on interfaces with rate- and state-dependent friction, *Proc. Math. Phys. Eng. Sci.* **472,** no. 2192, 20160,254, doi: 10.1098/rspa.2016.0254.

Ward, S. N. (2012). ALLCAL earthquake simulator, *Seismol. Res. Lett.* **83,** no. 6, 964–972, doi: 10.1785/0220120056.

Wei, M., Y. Kaneko, Y. Liu, and J. J. McGuire (2013). Episodic fault creep events in California controlled by shallow frictional heterogeneity, *Nature Geosci.* **6,** 566–570, doi: 10.1038/ngeo1835.

Wei, M., Y. Kaneko, P. Shi, and Y. Liu (2018). Numerical modeling of dynamically triggered shallow slow slip events in New Zealand by the 2016 Mw 7.8 Kaikoura earthquake, *Geophys. Res. Lett.* **45,** no. 10, 4764–4772.

Wollherr, S., A.-A. Gabriel, and P. M. Mai (2019). Landers 1992 "reloaded": Integrative dynamic earthquake rupture modeling, *J. Geophys. Res.* **124,** no. 7, 6666–6702.

Wollherr, S., A.-A. Gabriel, and C. Uphoff (2018). Off-fault plasticity in three-dimensional dynamic rupture simulations using a modal Discontinuous Galerkin method on unstructured meshes: Implementation, verification and application, *Geophys. J. Int.* **214,** no. 3, 1556–1584, doi: 10.1093/gji/ggy213.

Wu, Y., and X. Chen (2014). The scale-dependent slip pattern for a uniform fault model obeying the rate-and state-dependent friction law, *J. Geophys. Res.* **119,** no. 6, 4890–4906.

Xu, J., H. Zhang, and X. Chen (2015). Rupture phase diagrams for a planar fault in 3-d full-space and half-space, *Geophys. J. Int.* **202,** no. 3, 2194–2206.

Yang, H., S. Yao, B. He, A. V. Newman, and H. Weng (2019). Deriving rupture scenarios from interseismic locking distributions along the subduction megathrust, *J. Geophys. Res.* **124,** no. 10, doi: 10.1029/2019JB017541.

Manuscript received 5 September 2019
Published online 29 January 2020